Characterization of atmospheric turbulence effects over 149 km propagation path using multi-wavelength laser beacons

Mikhail A. Vorontsov
School of Engineering, University of Dayton, Dayton, Ohio 45469, USA
Gary W. Carhart
Computational and Information Sciences Directorate, U.S. Army Research Laboratory, Adelphi, Maryland 20783, USA
V. S. Rao Gudimetla
Directed Energy Directorate, Air Force Research Laboratory, Kihei, Maui, Hawaii 96753, USA
Thomas Weyrauch
School of Engineering, University of Dayton, Dayton, Ohio 45469, USA
Eric Stevenson
Boeing LTS, Kihei, Maui, Hawaii 96753, USA
Svetlana L. Lachinova
Institute for Systems Research, University of Maryland, College Park, Maryland 20742, USA
Leonid A. Beresnev
Computational and Information Sciences Directorate, U.S. Army Research Laboratory, Adelphi, Maryland 20783, USA
Jiang Liu
Computational and Information Sciences Directorate, U.S. Army Research Laboratory, Adelphi, Maryland 20783, USA
Karl Rehder
Boeing LTS, Kihei, Maui, Hawaii 96753, USA
and
Jim F. Riker
Space Vehicles Directorate, Air Force Research Laboratory, Kirtland AFB, New Mexico 87117, USA

ABSTRACT

We describe preliminary results of a set of laser beam propagation experiments performed over a long (149 km) near-horizontal propagation path between Mauna Loa (Hawaii Island) and Haleakala (Island of Maui) mountains in February 2010. The distinctive feature of the experimental campaign referred to here as the Coherent Multi-Beam Atmospheric Transceiver (COMBAT) experiments is that the measurements of the atmospheric-turbulence induced laser beam intensity scintillations at the receiver telescope aperture were obtained simultaneously using three laser sources (laser beacons) with different wavelengths ($\lambda_1 = 0.53$ μm, $\lambda_2 = 1.06$ μm, and $\lambda_3 = 1.55$ μm). The presented experimental results on intensity scintillation characteristics reveal complexity of the observed phenomena that cannot be fully explained based on the existing atmospheric turbulence models.

1. INTRODUCTION

There is a growing interest in development of optical systems capable of operation over long atmospheric distances (path lengths up to and over 100 km) in various atmospheric conditions and engagement scenarios. Among these systems are long-range laser communications, remote sensing, active and passive imaging, target tracking and designation, and laser beam projection (directed energy) systems. Propagation of optical waves over a long distance through volume atmospheric turbulence can result in significant changes in characteristics of received or transmitted waves and thus dramatically impact performance of the optical systems.

The turbulence effects over atmospheric propagation paths are commonly associated with fluctuations of intensity (scintillations), formation of wavefront phase topological singularities (branch points), wander and widening of laser beam, spatial non-uniformity of the turbulence-induced image degradation, etc. [1–4].

Currently, analysis of atmospheric turbulence-induced effects is based on theoretical and numerical models that are derived from the classical Kolmogorov-Obukhov turbulence theory [5–8], developed in 1940's–1960's. This theory was extensively validated through a number of various atmospheric experiments. The majority of these experiments were performed over relatively short distances (commonly with path lengths of less than several kilometers [9–12]) and only a few experiments over distances exceeding 100 km [13–15]. Nevertheless the models derived from the classical Kolmogorov-Obukhov turbulence theory are commonly used for performance assessment of long-range optical systems. The existing gap in experimental validation of turbulence models over long-range propagation distances may result in significant errors, leading to miscalculations of optical system capabilities and conceptual mistakes in their design.

The risk related with unconscious extension of the classic Kolmogorov-Obukhov turbulence model for analysis of atmospheric turbulence effect on optical wave propagation over long-range distances has been recognized and experimental evidence of noticeable deviations from this model prediction have already been observed in a few long-range experiments [13–16]. Several physical factors can contribute to such unanticipated (non-classical) behavior of optical wave characteristics that are not accounted for in the existing theories, including dynamics of large-scale air flows leading to strongly non-stationary refraction effects, impact of ocean-land interface, non-uniformity of air pressure, temperature, and wind profiles along the propagation path. Unfortunately, due to complexity (both logistical and technical) and cost which are commonly associated with long-range optical wave propagation experiments, the collected experimental data are not sufficiently representative to determine if some important adjustments can be made to the existing theory to account for extended turbulence effects, or if fundamentally new approaches are required.

In this paper we intend to partially fill out the existing gap in experimental assessment of extended turbulence effects on laser beam propagation over long-range paths by providing a large amount of intensity scintillation data obtained over a 149 km long propagation path using light sources with different wavelength.

The intensity scintillations are commonly characterized by the normalized variance of optical wave intensity fluctuations measured using a point photo-detector located at a point $\mathbf{r} = \{x,y\}$ of receiver aperture,

$$\sigma_I^2(\mathbf{r}) = \frac{\left\langle \left(I(\mathbf{r}) - \langle I(\mathbf{r}) \rangle \right)^2 \right\rangle}{\langle I(\mathbf{r}) \rangle^2}, \tag{1}$$

where $I(\mathbf{r})$ is the short-exposure intensity at the photo-detector point and angular brackets denote averaging over the ensemble of statistically independent realizations of refractive index perturbations of the propagation medium (atmospheric turbulence). It is assumed that random fluctuations of intensity are homogeneous and isotropic and hence the normalized variance $\sigma_I^2(\mathbf{r})$ in Eq. (1) is independent of coordinate vector $\mathbf{r}$, that is, $\sigma_I^2(\mathbf{r}) = \sigma_I^2$.

In accordance with the classical and more recent atmospheric turbulence theories, the normalized intensity scintillation variance σ_I^2 can be represented as

$$\sigma_I^2 = \lambda^{-7/6} F\left(C_n^2, l_0, L_0, z, h\right), \tag{2}$$

where λ is the wavelength of the propagating quasi-monochromatic wave and $F(C_n^2, l_0, L_0, z, h)$ is a factor represented here as a function of the propagation path characteristics (distance z and elevation h) and the major turbulence parameters: structure constant C_n^2, inner scale l_0, and outer scale L_0. The particular form of function $F(C_n^2, l_0, L_0, z, h)$ depends on theoretical models and approximations used to obtain expression (2) [17, 18].

In this respect, in principle, validity of one or another theoretical model can be tested through measurements of the intensity scintillation variance $\sigma_I^2(\mathbf{r})$ and independent calculation of the factor $F(C_n^2, l_0, L_0, z, h)$ in Eq. (2). Nevertheless, such an approach requires knowledge of the propagation path and turbulence characteristics the function $F(C_n^2, l_0, L_0, z, h)$ depends on. In practice, these parameters cannot be measured independently and directly.

This problem however can be overcome using simultaneous measurements of intensity scintillations corresponding to optical waves at different wavelengths that are originating from a single laser beacon and hence propagating along identical atmospheric path. As follows from Eq. (2), the ratio of the normalized variances $\sigma_I^2(\lambda_1)$ and $\sigma_I^2(\lambda_2)$ corresponding to the laser beacon wavelengths λ_1 and λ_2 represents a value independent of the factor $F(C_n^2, l_0, L_0, z, h)$: $\sigma_I^2(\lambda_1)/\sigma_I^2(\lambda_2) = (\lambda_2/\lambda_1)^{7/6}$.

The idea of atmospheric turbulence characterization using multi-wavelength laser beacons with simultaneous measurements of intensity scintillations at different wavelengths has been implemented in the COMBAT experiments. In these experiments intensity scintillations were simultaneously measured using three closely located identical laser beacons that generated truncated Gaussian beams at the following wavelengths: $\lambda_1 = 0.53$ μm, $\lambda_2 = 1.06$ μm, and $\lambda_3 = 1.55$ μm. To simplify notations, the corresponding beacons are referred to as green (G), infra-red (IR), and laser communications (COM) beacons. In accordance with Eq. (2), the ratios of the corresponding intensity scintillation variances expected from the atmospheric turbulence theory, $R^T_{\mathrm{G/IR}}$, $R^T_{\mathrm{G/COM}}$, and $R^T_{\mathrm{IR/COM}}$, are given by

$$R^T_{\mathrm{G/IR}} = \frac{\sigma_I^2(0.53\,\mu\mathrm{m})}{\sigma_I^2(1.06\,\mu\mathrm{m})} = 2.24; \quad R^T_{\mathrm{G/COM}} = \frac{\sigma_I^2(0.53\,\mu\mathrm{m})}{\sigma_I^2(1.55\,\mu\mathrm{m})} = 3.50; \quad R^T_{\mathrm{IR/COM}} = \frac{\sigma_I^2(1.06\,\mu\mathrm{m})}{\sigma_I^2(1.55\,\mu\mathrm{m})} = 1.56\,. \tag{3}$$

In the COMBAT experiments, the experimental values of the ratios $R^E_{\mathrm{G/IR}}$, $R^E_{\mathrm{G/COM}}$, and $R^E_{\mathrm{IR/COM}}$ corresponding to Eq. (3) were directly obtained using simultaneous measurements of statistically representative ensembles of short-exposure intensity patterns $I(\mathbf{r}, \lambda_1)$, $I(\mathbf{r}, \lambda_2)$, and $I(\mathbf{r}, \lambda_3)$ inside the receiver telescope aperture of diameter 90 cm located a distance 149 km from the corresponding laser beacons. With the understanding that over long propagation paths the assumptions of stationary and isotropic turbulence with homogeneous statistics – the basis for the Kolmogorov-Obukhov turbulence theory – are not always satisfied, we expected some deviation in values between the ratios $R^T_{\mathrm{G/IR}}$, $R^T_{\mathrm{G/COM}}$, and $R^T_{\mathrm{IR/COM}}$ in Eq. (3), as predicted by the theory, and the values $R^E_{\mathrm{G/IR}}$, $R^E_{\mathrm{G/COM}}$, and $R^E_{\mathrm{IR/COM}}$ obtained experimentally. The real surprise was the degree of disconnect between predictions based on homogeneous turbulence theory and measurements as illustrated by the data obtained and discussed below.

2. COMBAT EXPERIMENTAL SETTING

Laser beam propagation experiments were performed over the propagation path of length $L \cong 149.2$ km between the laser beacon platform located on the Mauna Loa mountain (Hawaii island) at elevation $h_{\mathrm{ML}} = 3397$ m (11,140 ft), and the 3.67-m receiver telescope on the top of the Haleakala mountain (Maui island) at elevation $h_{\mathrm{H}} = 3058$ m (see Fig. 1). Due to the Earth's curvature, the minimum height along the propagation path $h_{\min} \cong 2775$ m corresponds to the distance 60 km from the receiver site.

The laser beacon assembly at the Mauna Loa Observatory comprised three single-mode fiber collimators (each with a clear aperture of 26 mm) and the corresponding lasers: a fiber-coupled laser diode at the wavelength of $\lambda_1 = 0.532$ μm and two fiber lasers with wavelengths of $\lambda_2 = 1.064$ μm and $\lambda_3 = 1.55$ μm. The fiber collimators were

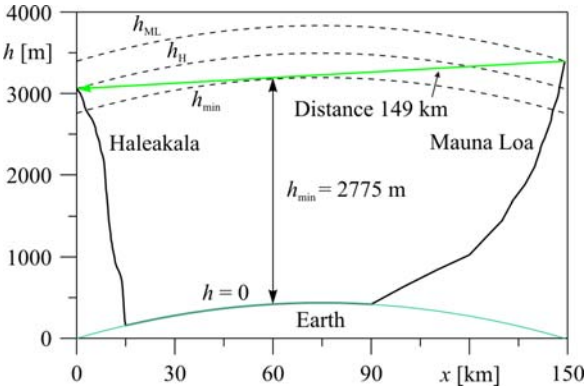

Fig. 1. Elevation profile along the propagation path from the Mauna Loa NOAA observatory to the AEOS telescope on Haleakala.

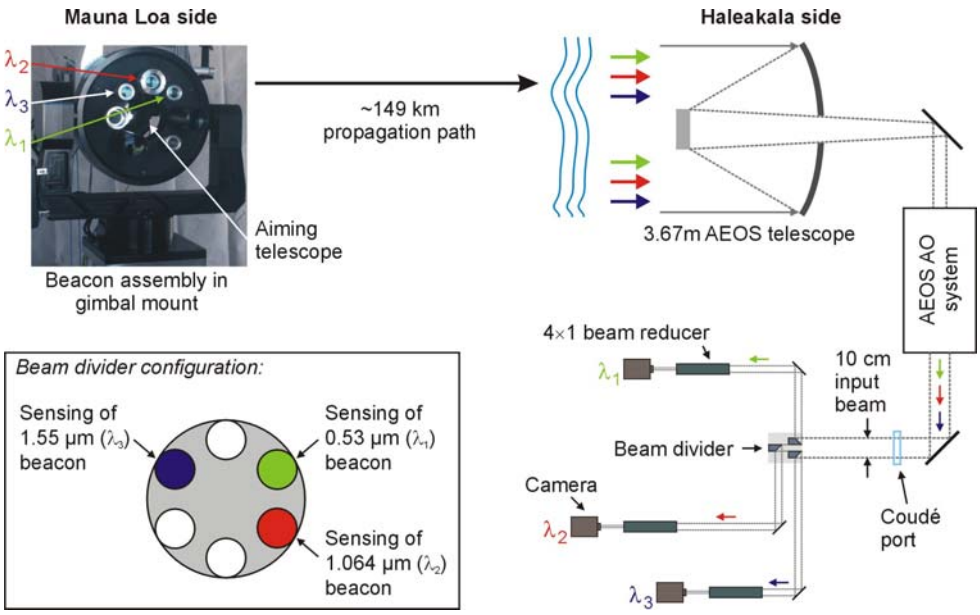

Fig. 2. Conceptual schematic of the COMBAT experimental system.

mounted together with an aiming telescope into a gimbal system (see Fig. 2), which allowed for pointing with a smallest angular step size of 1.75 μrad, corresponding to a lateral beam deflection of 26 cm at the receiver telescope over 149 km distance. Each fiber collimator had means for manual horizontal, vertical, and axial alignment of the fiber tip with respect to the collimating lens to adjust beam pointing and focus. For co-alignment of the fiber collimators' optical axes with the aiming telescope, a corner-cube retro-reflector was mounted in front of the beacon assembly in such way that some part of the light from two collimators at a time was directed into the aiming telescope and focused onto the camera surface located in its focal plane. Using the 1064 nm collimator as reference, the focal spots of all three beams were brought to coincide in the telescope focus, which in turn co-aligned the collimated beams. After the alignment procedure, the retro-reflector was removed and the beacon assembly was pointed toward the receiver telescope [3.67 m Air Force Advanced Electro-Optical System (AEOS telescope)] using the beams' former spot location in the camera's field-of-view as aimpoint. A searchlight installed in front of the AEOS telescope helped to achieve and maintain correct aiming after sunset, when the telescope was no longer visible with the aiming telescope.

Another search light installed near the beacon assembly at the Mauna Loa Observatory allowed for alignment of the AEOS telescope toward the beacons. After propagation to Maui site, the optical waves from the beacons were received by the AEOS telescope and sent through the coudé path to the deformable mirror, which is part of the AEOS adaptive optics system operating in the visible wavelength band. The adaptive optics system was off and the deformable mirror was flattened during the experiments. Collimated light from the adaptive optics bench (beam diameter 10 cm) was sent to one of the AEOS coudé rooms where the beam was subdivided into six separate subapertures, each having a usable diameter of 25 mm (Fig. 2). Each subaperture corresponds to an area with a diameter of 91.7 cm at the telescope pupil considering the de-magnification of the receiver area from 3.67 m diameter at the telescope's primary mirror to 10 cm in the coudé room. Three of the subapertures were used to record pupil-plane and focal-plane irradiance distributions of the received beams (Fig. 2). Narrow bandpass filters were used to dedicate each subaperture to a specific wave from a single beacon. In this paper we discuss only measurements of the pupil-plane intensity distributions, which were recorded using three Sensors Unlimited (SU640SDWHvis) 14-bit cameras. The cameras were operating in a windowed mode with 256×256 pixels' window, providing an actual sensor area of 6.4×6.4 mm^2 with a pixel size of 25×25 μm^2 and a 100% fill factor. A four-to-one beam reducer was installed in the optical train of each subaperture to match the beam (pupil) size with the active window size.

3. MEASUREMENTS AND RESULTS

3.1 Data Recording and Processing

The COMBAT measurements were performed from early evening to middle night from Feb. 12 to Feb. 21, 2010. Data collection consisted of a set of experimental trials (typically from 10 to 30) between 7:00 p.m. and 11:30 p.m. during each night of measurements. During each trial a set of nearly 10000 frames of short-exposure intensity patterns in the form of 14-bit digital arrays $\{I_n(\mathbf{r}_{m,l},\lambda_1)\}$, $\{I_n(\mathbf{r}_{m,l},\lambda_2)\}$, and $\{I_n(\mathbf{r}_{m,l},\lambda_3)\}$ were recorded simultaneously using three identical cameras located in the image planes of the telescope subapertures that are dedicated to each beacon. Here n is the frame number in the experimental trial ($n = 1, \ldots, 9980$), $\mathbf{r}_{m,l}$ is the transversal coordinate vector in the plane of photo-array ($m,l = 1, \ldots, 256$), and λ_q is the received light wavelength ($q = 1, 2, 3$). The time of the first frame capture by all cameras within each trial was triggered from a PC computer. The capture rate (between 200 and 350 frames per second dependent on the trial) and the integration time (between 1 ms and 2 ms) were identical for all cameras. The averaged deviation between capturing of intensity patterns $I_n(\mathbf{r}_{m,l},\lambda_1)$, $I_n(\mathbf{r}_{m,l},\lambda_2)$, and $I_n(\mathbf{r}_{m,l},\lambda_3)$ by different cameras did not exceed 1.0 ms. The physical size of the camera's pixel 25×25 μm^2 corresponds to the telescope receiver aperture size of approximately 3.6×3.6 mm^2. Thus the measurements obtained at each pixel of the photo-array correspond to the received light intensity averaged over 3.6-mm square aperture in the AEOS telescope pupil plane. According to the camera specification, variation in sensitivity from pixel to pixel did not exceed 1% and therefore was neglected. To avoid aperture boundary effects related with small amplitude slow displacement of the received beam centroid during the time of measurements, the intensity scintillation data were analyzed inside the circle area corresponding to the sub-aperture boundary reduced by 10 pixels of the photo-array.

To exclude the data recorded by photo-array pixels that are not properly functioning (broken or blocked by presence of dust on optics or sensor), the following procedure was applied. For each measurement trial we calculated variance of the intensity fluctuations at each pixel

$$\sigma_{pix}^2\left(\mathbf{r}_{m,l}\right) = \left\langle \left[I_n\left(\mathbf{r}_{m,l}\right) - \overline{I}_n \right]^2 \right\rangle_N , \tag{4}$$

where $\overline{I}_n = N^{-1}\sum_{n=1}^{N} I_n(\mathbf{r}_{m,l})$ is the averaged value of pixel intensity corresponding of the set of N short-exposure images belonging to a single measurements trial. The pixels were excluded in the further analysis if the corresponding values of the intensity fluctuation variance $\sigma_{pix}^2\left(\mathbf{r}_{m,l}\right)$ for these pixels were less than 1% from the aperture-average value. In addition, we performed the camera offset correction by capturing a "dark map" for each of the cameras at the beginning of each data collection trial. The values of the "dark map" images were then subtracted from all subsequent data frame captures. The dark maps were recorded by blocking all external light from entering the optical system at the experiment room's coudé port. However, this dark map capture procedure does not take into account any external background light such as the light from the sky, which should also be removed. The impact of this external background light was removed by calculating a map of minimum intensities detected during each trial for each pixel. This "min map" data was subtracted from all the frames of the trial. Note that the difference in the intensity variance (4) brought about by using this additional min map correction or not only produces a change of a few percent in its value and the true value must lie in the range between the two possibilities. It is believed that most of the min map detected intensity is in fact sky background illumination and therefore the data presented makes use of the min map correction.

3.2 Received Power Fluctuations

Intensity scintillations observed during most of experiments were surprisingly strong. The short-exposure intensity patterns show the presence of speckles of very different spatial scales: from few centimeters or less to large speckles of approximately the size of the receiver aperture (~0.9 m). These large-size speckles were seen as spikes and deep fadings in the received optical power signal. In most experiments the intensity scintillation patterns did not show coherent (directional) motion but rather random appearance and disappearance. As rare exceptions in windy conditions at the receiver site, we observed occasional coherent motion of small-scale speckles.

Consider first the received light power fluctuations data simultaneously recorded for all three beacons. For each short-exposure intensity pattern (image frame), the optical power averaged over the aperture is defined as

$$P_n = \sum_{m}^{M} I_n\left(\mathbf{r}_m\right), \tag{5}$$

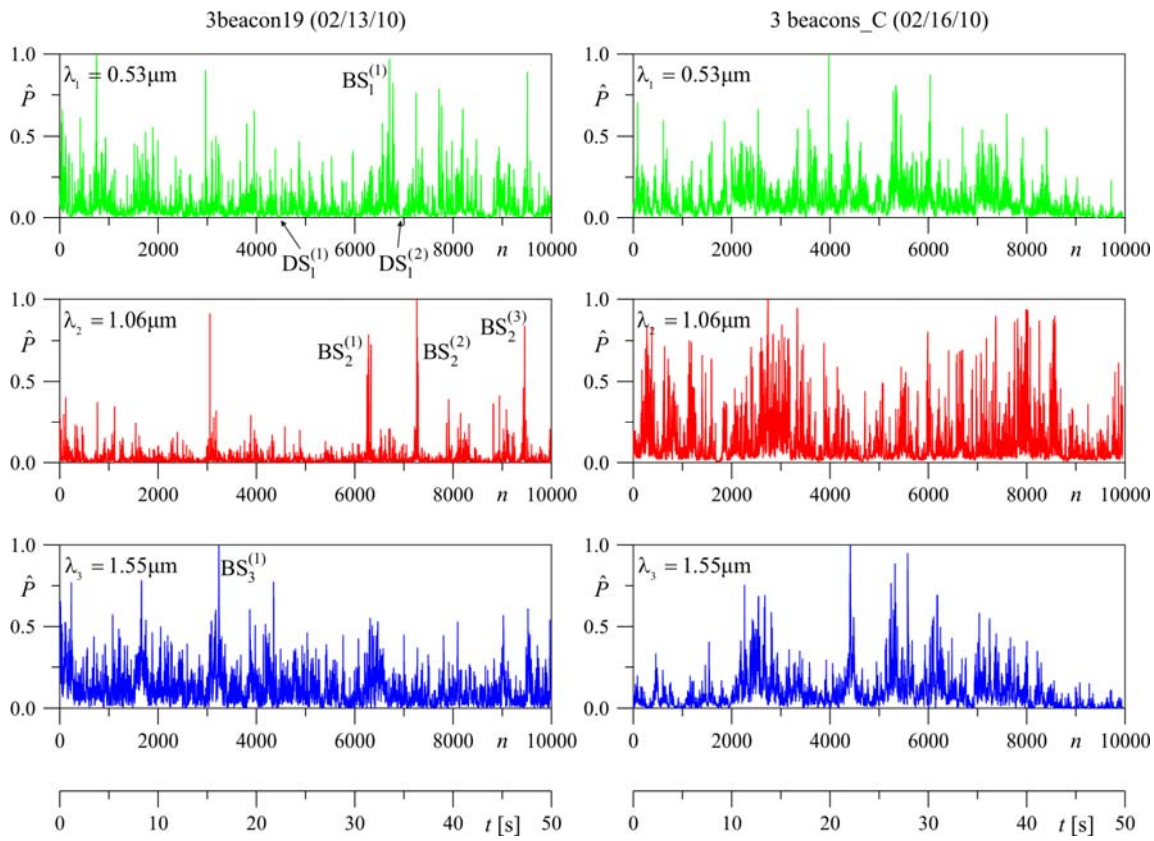

Fig. 3. Temporal dynamics of received optical power fluctuations $\hat{P} = P_n / \max_n P_n$ for laser beacons with wavelengths $\lambda_1 = 0.53$ μm (top, green), $\lambda_2 = 1.06$ μm (middle, red), and $\lambda_3 = 1.55$ μm (bottom, blue) corresponding to the experimental trials labeled as "3beacon19" (left column) and "3 beacon_C" (right column). The date and recording time are shown on the top of each column. During each trial, three sequences of 10000 short-exposure frames with 2 ms integration time were captured simultaneously. Several selected bright and dark spikes in the received power for the trial "3beacon19" are shown by BS and DS marks. The amplitudes of the biggest spikes in the data set "3beacon19" are: $P_{\lambda_1}^{\max} = 14.8\overline{P}_{\lambda_1}$ (green beacon), $P_{\lambda_2}^{\max} = 40.0\overline{P}_{\lambda_2}$ (IR beacon) and $P_{\lambda_3}^{\max} = 8.7\overline{P}_{\lambda_3}$ (COM beacon). Here $\overline{P}_{\lambda_1}$, $\overline{P}_{\lambda_2}$, and $\overline{P}_{\lambda_3}$ are the averaged received power values for each wavelength.

where $M = 256\times256$. To simplify notation, in Eq. (5) and below we use a single index m to denote the camera pixel coordinate vector. The dependencies of the normalized power $\hat{P}(n)$ on the consequent frame number n or physical time t are shown in Fig. 3 for two representative measurements trials. In this figure, we can clearly see the presence of large spikes on the received power which indicate the occasional appearance of large-size bright and dark speckles at the receiver aperture for all three wavelengths. Bright speckles can result in up to ten-fold increase in received power. Note that for the "3beacon19" trial with $\lambda_2 = 1.06$ μm (red), the amplitude of spikes appeared to be drastically higher. The appearance of large-amplitude bright or dark spikes in received power can be explained by the existence of slowly changing/moving large-scale coherent structures of refractive index that play a role of large aperture lenses with several kilometer-long focal lengths. As can be seen from Fig. 3, there seems to be no correlation between the appearance of bright and dark speckles for laser beacons of different wavelengths.

The characteristic snapshots of the received light pupil-plane intensity distributions for beacons with different wavelengths are illustrated in Fig. 4. The snapshots are chosen from the vicinities of bright spikes $\mathrm{BS}_1^{(1)}$, $\mathrm{BS}_2^{(1)}$, and $\mathrm{BS}_3^{(1)}$ indicated in Fig. 3. The images in Fig. 4 show that the spatial scale of intensity scintillations is strongly dependent on the wavelength, i.e., the larger the wavelength the larger the speckles. This observation is consistent

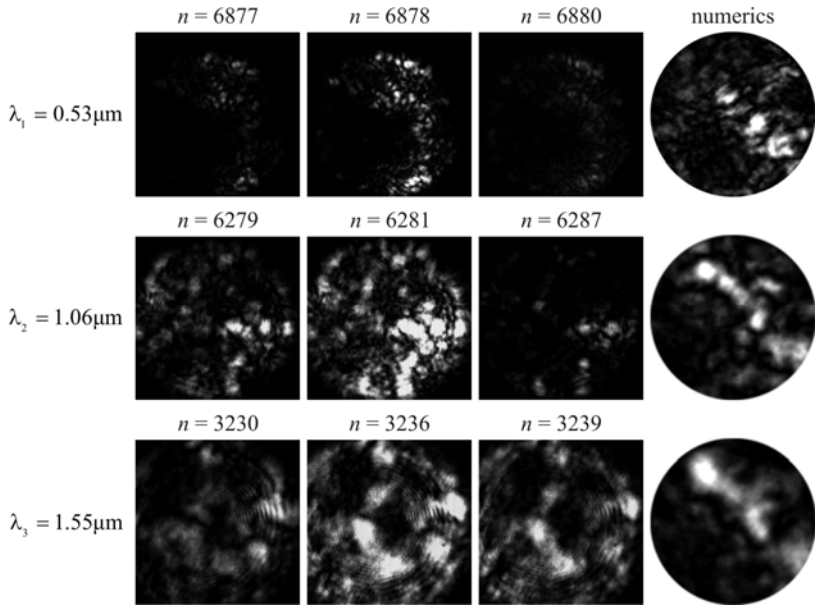

Fig. 4. Snapshots of pupil-plane intensity distributions of received light, $I_n(\mathbf{r}_m)$, from beacons with three different wavelengths, $\lambda_1 = 0.53$ μm, $\lambda_2 = 1.06$ μm, and $\lambda_3 = 1.55$ μm, for "3beacon19" measurement trial. First three columns represent experimental data; frame numbers n are denoted above the intensity images. Last column contains typical snapshots of intensity distributions within a single subaperture obtained numerically.

with the theoretical findings and was also confirmed by our numerical simulations (see the most right column in Fig. 4).

3.3 Intensity Scintillations

Spatial non-uniformity of intensity in each short-exposure intensity pattern (frame) of a trial can be characterized by the set of values (one per a single frame) referred to here as spatial variances

$$\sigma_S^2(n) = \left\langle \left[I_n(\mathbf{r}_m) - \overline{I}_n \right]^2 \right\rangle_S \Big/ \overline{I}_n^2 , \tag{6}$$

where $\overline{I}_n = M^{-1} \sum_{m=1}^{M} I_n(\mathbf{r}_m)$ is the aperture-average intensity for the nth frame. The index S in Eq. (6) denotes averaging over spatial coordinate (over pixels). The sequence of $\sigma_S^2(n)$ values characterizes temporal changes of spatial variance occurring during the time of measurements trial. Correspondingly, by averaging $\sigma_S^2(n)$ over the set of N samples, which corresponds to time averaging, we obtain statistical characteristic $\sigma_{SN}^2 = \left\langle \sigma_S^2(n) \right\rangle_N$ that can be used for evaluation of spatial non-uniformity of intensity for the entire trial. Dependencies $\sigma_S^2(n)$ for three different wavelengths and two measurement trials are shown in Fig. 5. The averaged values σ_{SN}^2 are given inside the corresponding plots.

Another and more commonly used approach for intensity scintillations analysis is based on computation of the normalized variance of intensity fluctuations at a single photo-array pixel,

$$\sigma_N^2(\mathbf{r}_m) = \left\langle \left[I_n(\mathbf{r}_m) - \overline{I}(\mathbf{r}_m) \right]^2 \right\rangle_N \Big/ \overline{I}^2(\mathbf{r}_m) , \tag{7}$$

where $\overline{I}(\mathbf{r}_m) = 1/N \sum_{n=1}^{N} I_n(\mathbf{r}_m)$. The averaging over the set of $N \approx 10000$ frames in Eq. (7) is equivalent to time averaging over nearly 50 seconds. The normalized variance (7) is referred to as the scintillation index. By averaging $\sigma_N^2(\mathbf{r}_m)$ over all pixels inside the receiver aperture (with exception of "bad" pixels described above) we obtain the aperture-average scintillation index $\sigma_{NS}^2 = \left\langle \sigma_N^2(\mathbf{r}_m) \right\rangle_S$.

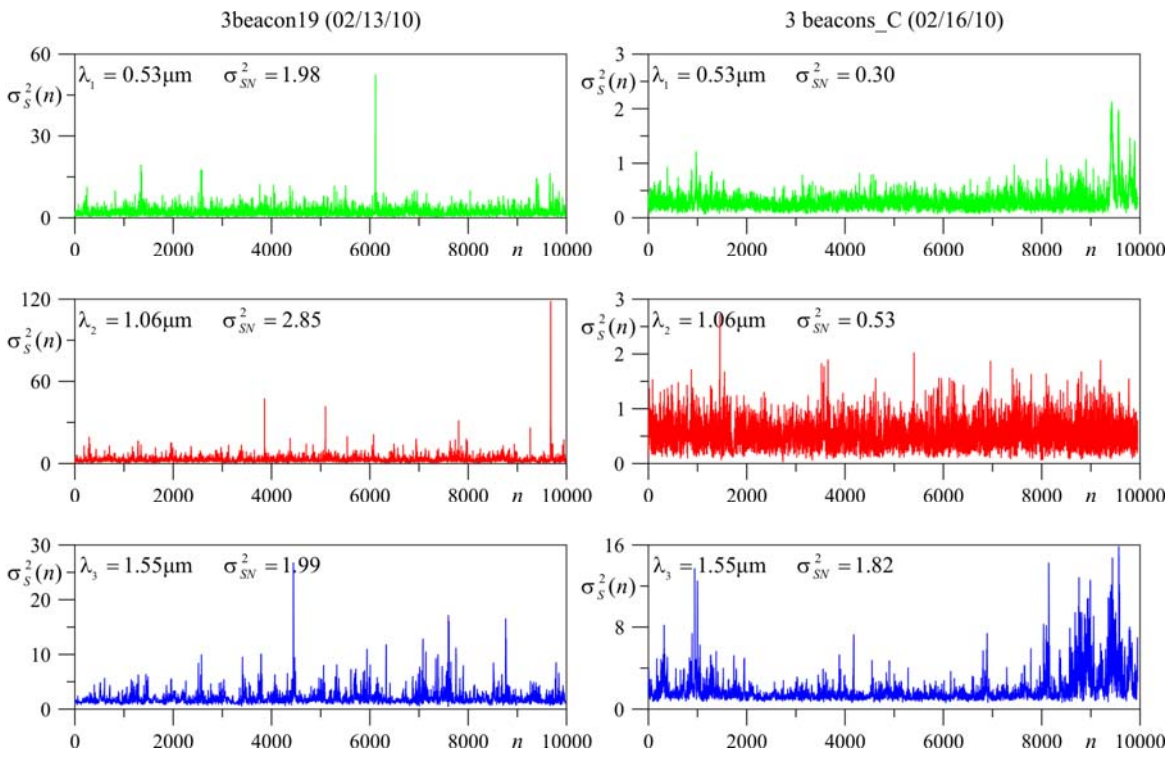

Fig. 5. Spatial variances of short-exposure intensity non-uniformity inside receiver subaperture, σ_S^2, as functions of frame number n for "3beacon19" (left) and "3 beacon_C" (right) measurement trials and three wavelengths, $\lambda_1 = 0.53$ μm (top, green), $\lambda_2 = 1.06$ μm (middle, red), and $\lambda_3 = 1.55$ μm (bottom, blue).

In order to evaluate whether the observed intensity scintillations can be considered as a stationary random process, consider analogues of the scintillation index obtained using either increasing number n of subsequent frames $\sigma_{nS}^2(n)$ or "moving" (window) averaging of n sequential frames $\sigma_{WS}^2(n, n_W)$, where n_W is a number of frames in the selected averaging window. Both $\sigma_{nS}^2(n)$ and $\sigma_{WS}^2(n)$ dependencies are shown in Fig. 6; the values σ_{NS}^2 are given inside the corresponding plots.

The gray-scale images shown at the bottom of Fig. 6 illustrate spatial non-uniformity of the scintillation index $\sigma_N^2(\mathbf{r}_m)$ obtained by averaging different number of frames in the trial for different beacons. The indication of spatial homogeneity of intensity scintillation process is spatial uniformity of the images mapping scintillation index $\sigma_N^2(\mathbf{r}_m)$. As it can be seen from $\sigma_N^2(\mathbf{r}_m)$-images in Fig. 6, averaging over 10000 frames results in quite uniform $\sigma_N^2(\mathbf{r}_m)$-images for the "3 beacon_C" measurement trial, while the corresponding $\sigma_N^2(\mathbf{r}_m)$-images for the "3beacon19" trials are still highly non-uniform. This indicates statistical non-stationary character of the intensity scintillation process during this measurement trial. The same conclusion regarding non-stationary character of the scintillation process can be also derived from the analysis of dependencies of $\sigma_{nS}^2(n)$ and $\sigma_{WS}^2(n, n_W)$ in Fig. 6. This highly non-stationary behavior of the scintillations can be associated with the presence of the large-scale intensity scintillations components (large-scale bright and dark speckles).

Assuming that the ergodic hypothesis can be applied, the obtained values σ_{SN}^2 and σ_{NS}^2 should be approximately equal since they are obtained by changing the order of spatial and temporal averaging [15]. However, when comparing the corresponding values σ_{SN}^2 and σ_{NS}^2 calculated for the two selected data sets (trials) in Figs. 5 and 6, we see that these values are quite different and so application of the ergodic hypothesis is questionable.

Bar diagrams summarizing the results for σ_{SN}^2 and σ_{NS}^2 obtained for a number of measurement trials during the COMBAT experimental campaign along with the wave-optics simulation results are shown in Fig. 7. Bars' heights

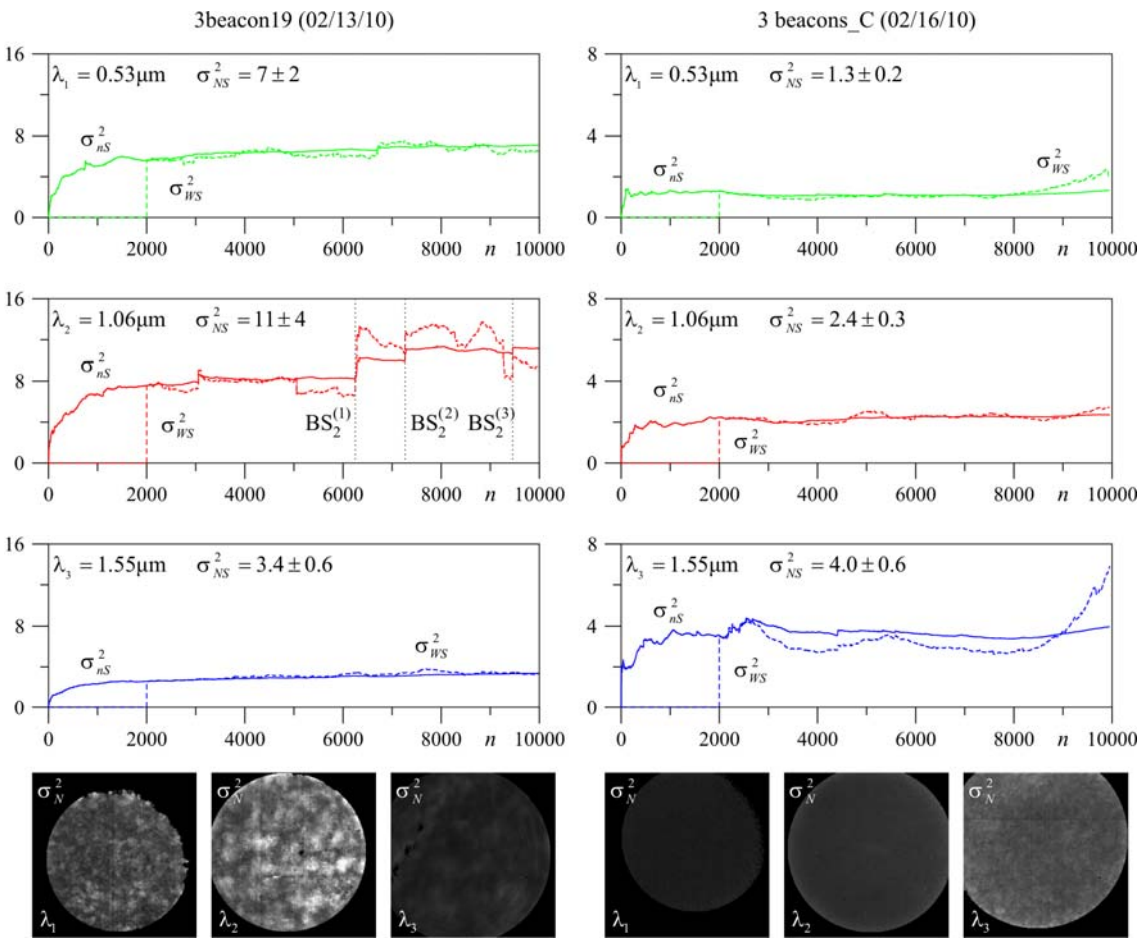

Fig. 6. Evolution of the aperture-average scintillation indices $\sigma^2_{nS}(n)$ (solid lines) and $\sigma^2_{WS}(n, n_W)$ for $n_W = 2000$ (dashed lines) for three different wavelengths, $\lambda_1 = 0.53$ μm (top, green), $\lambda_2 = 1.06$ μm (middle, red), and $\lambda_3 = 1.55$ μm (bottom, blue), and for "3beacon19" (left), and "3 beacon_C" (right). Corresponding intensity variance images, $\sigma^2_N(\mathbf{r}_m)$, are shown at the bottom.

indicate spatial variance σ^2_{SN} (top) and scintillation index σ^2_{NS} (bottom) values, while color of the bars denote the wavelength of the laser beacons used in experiments, i.e., $\lambda_1 = 0.53$ μm (green), $\lambda_2 = 1.06$ μm (red), and $\lambda_3 = 1.55$ μm (blue) beacons, respectively. Each set of adjacent green, red, and blue bars corresponds to a different measurement trial whose name is indicated below the set; numbers at the tops of each set denote local time of the experiment. Groups of several sets of bars correspond to different dates of the experiments, specified below the diagram. Numerical simulation results obtained for the HV-5/7 altitude profile model of refractive index structure parameter (see, e.g., [19]) are shown by the first group of bars.

Several conclusions can be drawn from the comparison of the experimental with the numerical simulation data. First, the experiments showed significantly (2–4 times) larger scintillation index values. Second, contrary to the predictions indicated by the wave optics simulation results, the scintillation index for 1.06 μm laser beam (red bars) was noticeably larger than the one for the shorter wavelength beacon (0.53 μm, green bars) in almost all experiments.

In addition, using the numerical simulation and experimental data presented in Fig. 7, we computed the ratios of intensity scintillation variances (indices) $R^E_{\mathrm{G/IR}}$, $R^E_{\mathrm{G/COM}}$, and $R^E_{\mathrm{IR/COM}}$ as defined by Eq (3). In Table 1 the obtained from two measurement trials ratios $R^E_{\mathrm{G/IR}}$, $R^E_{\mathrm{G/COM}}$, and $R^E_{\mathrm{IR/COM}}$ are compared with the corresponding theoretical values $R^T_{\mathrm{G/IR}}$, $R^T_{\mathrm{G/COM}}$, and $R^T_{\mathrm{IR/COM}}$ obtained based on the expression (2) that describes the wavelength dependence

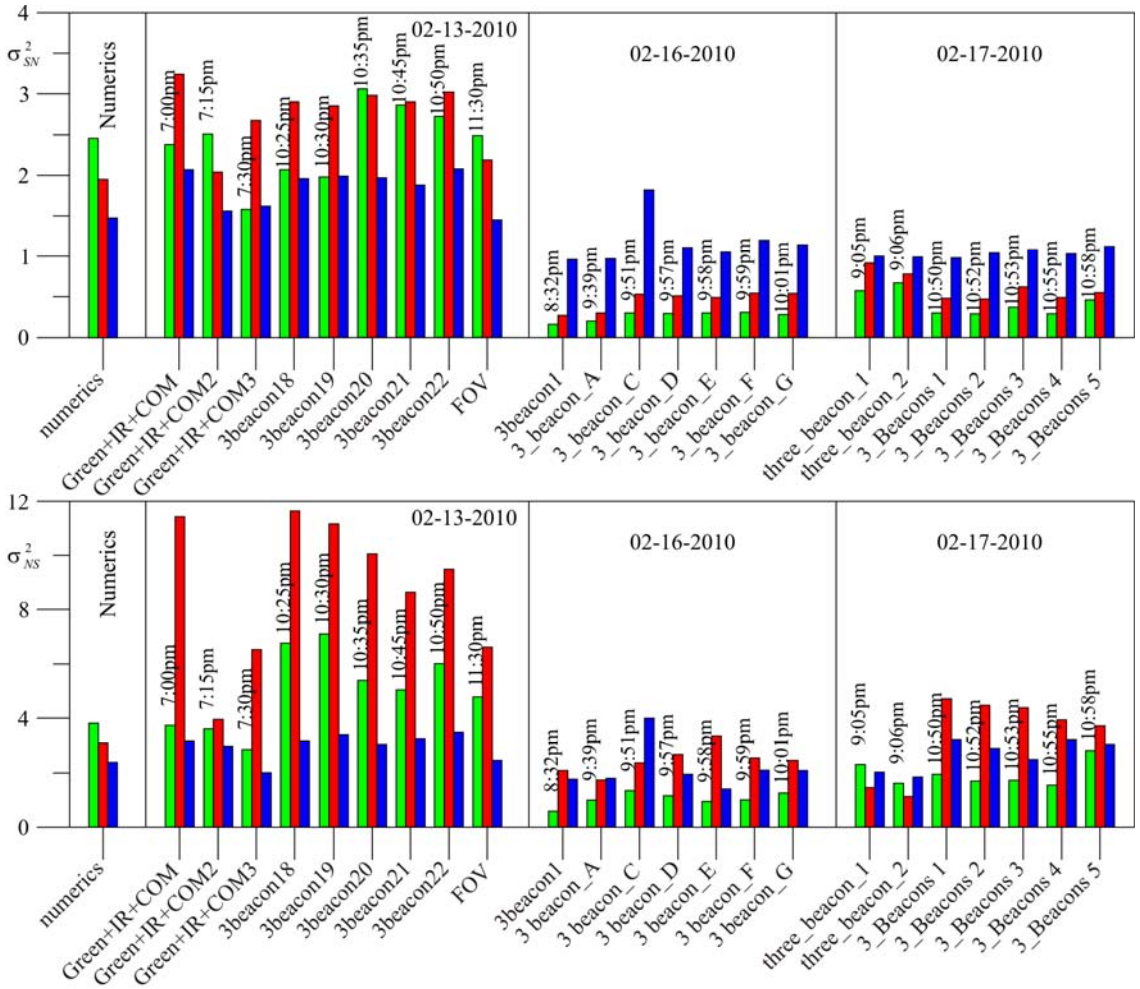

Fig. 7. Bar diagram summarizing experimental results for a large set of experimental trials obtained during three days (nights) of measurements during COMBAT experimental campaign for intensity scintillation spatial variances σ^2_{SN} (top) and intensity scintillation indices σ^2_{NS} (bottom) for three different wavelengths, $\lambda_1 = 0.53$ μm (green), $\lambda_2 = 1.06$ μm (red), and $\lambda_3 = 1.55$ μm (blue).

of the normalized intensity scintillation variance in accordance with the classical and more recent atmospheric turbulence theories. As can be seen from Table 1, the ratios of the intensity scintillation variances for different wavelengths [cf. Eq. (3)] computed using both numerical simulation and experimental data do not match those expected from theoretical calculations.

Table 1. Ratios of scintillation indices for different wavelengths.

	$R_{G/IR}$	$R_{G/COM}$	$R_{IR/COM}$
Theory [Eq. (3)]	2.24	3.50	1.56
"numerics"	1.23	1.60	1.29
"3beacon19"	0.64	2.11	3.31
"3 beacon_C"	0.57	0.34	0.59

4. SUMMARY

Results of the COMBAT experiments make questionable the assumption that stationary and isotropic turbulence with homogeneous statistics is valid for long-range propagation paths. Statistical characteristics of the observed intensity scintillation patterns (spatial and temporal) are highly diverse and dependent on local weather conditions and global coherent structures of temperature gradient dynamics along the propagation path. In most experiments the intensity scintillation and spatial variances measured exceeded by 2–4 times the corresponding values obtained using both analytics and numerical simulations based on the classical Kolmogorov-Obukhov turbulence model.

The observed intensity scintillation patterns for 149-km near-horizontal propagation are characterized by the increased appearance of both large (~1 m) and small (< 10 mm–5 mm) speckles. Their appearance can be associated with the presence of strong turbulent layers near the transmitter (large-scale speckles) and receiver (small-scale speckles). The frequent (0.3 s–1.0 s) appearance of large-amplitude spikes in received power indicates the existence of slowly changing/moving large-scale coherent structures with sharp refractive index changes at their boundaries.

In all experiments the intensity scintillation patterns do not show coherent (directional) motion but rather random appearance and disappearance. As rare exceptions in windy conditions at the receiver site, we observed occasional coherent motion of small-scale speckles. These results challenge the assumption of "frozen" turbulence (Taylor hypothesis) commonly used in analyses. In addition, the existence of numerous well-developed small-scale speckles makes the possibility of active/adaptive compensation questionable.

For the three-wavelength beacons (0.53 μm, 1.06 μm and 1.55 μm), the wavelength dependence of the intensity scintillation variance does not follow existing assumptions that the longer the wavelength the less the turbulence effect on the laser beam. Among other "anomalies" observed in the experiments are the mismatches between the predicted and the measured aperture-averaging factor and spatial autocorrelation functions (not discussed in this paper).

5. ACKNOWLEDGEMENTS

This project was supported through the HEL Joint Technology Office contract and the Cooperative Agreements between the US Army Research Laboratory and both the University of Dayton and University of Maryland. The authors also want to thank Dr. John Barnes (Mauna Loa Observatory/NOAA), Ms. Laura Ulibarri (AFRL Maui Branch Chief), Dr. Skip Williams (AFRL Maui Deputy Branch Chief), Bob Lytle, Kevin Moore, Ed Walker, Sarah Loney, Eddie Kanai (all Boeing, Maui) for support for the experimental campaigns.

6. REFERENCES

[1] V. I. Tatarskii, *The Effects of the Turbulence Atmosphere on Wave Propagation*. Jerusalem: Israel Program for Scientific Translations, 1971.

[2] V. E. Zuev, *Propagation of visible and infrared radiation in the atmosphere*. New York: John Wiley & Sons, 1974.

[3] A. Ishimaru, *Wave Propagation and Scattering in Random Media*. New York: Academic Press, 1978.

[4] D. L. Fried and J. L. Vaughn, "Branch cuts in the phase function," *Appl. Optics*, vol. 31, no. 15, pp. 2865–2882, 1992.

[5] A. N. Kolmogorov, "The local structure of turbulence in incompressible viscous fluid for very large Reynolds numbers," *Dokl. Akad. Nauk SSSR*, vol. 30, no. 4, pp. 299–303, 1941, [English translation in *Turbulence: Classic Papers on Statistical Theory* (ed. S. K. Friedlander and L. Topper), pp. 151–155. Interscience, New York, 1961].

[6] A. M. Obukhov, "On the distribution of energy in the spectrum of turbulent flow," *Dokl. Akad. Nauk SSSR*, vol. 32, no. 1, pp. 22–24, 1941.

[7] V. I. Tatarskii, *Wave Propagation in a Turbulent Medium*, ser. McGraw-Hill Series in Electrical Engineering. New York: McGraw-Hill, 1961.

[8] S. M. Rytov, Y. A. Kravtsov, and V. I. Tatarskii, *Principles of Statistical Radiophysics IV: Wave Propagation Through Random Media*. Berlin: Springer-Verlag, 1989.

[9] M. E. Gracheva and A. S. Gurvich, "Strong fluctuations in the intensity of light propagated through the atmosphere close to the Earth," *Izv. Vyssh. Uchebn. Zaved. Radiofiz.*, vol. 8, no. 4, pp. 711–724, 1965, [Radiophys. Quantum Electron., vol. 8, no. 4, 511–515 (1965)].
[10] W. A. Coles and R. G. Frehlich, "Simultaneous measurements of angular scattering and intensity scintillation in the atmosphere," *J. Opt. Soc. Am.*, vol. 72, no. 8, pp. 1042–1048, 1982.
[11] R. L. Phillips and L. C. Andrews, "Measured statistics of laser-light scattering in atmospheric turbulence," *J. Opt. Soc. Am.*, vol. 71, no. 12, pp. 1440–1445, 1981.
[12] A. Consortini, F. Cochetti, J. H. Churnside, and R. J. Hill, "Inner-scale effect on irradiance variance measured for weak-to-strong atmospheric scintillation," *J. Opt. Soc. Am. A*, vol. 10, no. 11, pp. 2354–2362, 1993.
[13] W. A. Bernard, B. M. Welsh, M. C. Roggemann, and R. J. Feldmann, "Atmospheric turbulence characterization of a low-altitude long horizontal path," in *Image Propagation through the Atmosphere*, Proc. SPIE vol. 2828, 198–209, C. Dainty and L. R. Bissonnette, Eds. Bellingham, Wash.: SPIE, 1996.
[14] N. Perlot, D. Giggenbach, H. Henniger, J. Horwath, M. Knapek, and K. Zettl, "Measurements of the beam-wave fluctuations over a 142 km atmospheric path," in *Free-Space Laser Communications VI*, Proc. SPIE vol. 6304, 63041O, A. K. Majumdar and C. C. Davis, Eds. Bellingham, Wash.: SPIE, 2006.
[15] W. M. Hughes and R. B. Holmes, "Pupil-plane imager for scintillometry over long horizontal paths," *Appl. Optics*, vol. 46, no. 29, pp. 7099–7109, 2007.
[16] M. S. Belen'kii, E. Cuellar, K. A. Hughes, and V. A. Rye, "Preliminary experimental evidence of anisotropy of turbulence at Maui Space Surveillance Site," in *Proceedings of the 2006 AMOS Conference*, S. Ryan, Ed., 2006, pp. 538–547.
[17] R. S. Lawrence and J. W. Strohbehn, "A survey of clear-air propagation effects relevant to optical communications," *Proc. IEEE*, vol. 58, no. 10, pp. 1523–1545, 1970.
[18] R. J. Hill and R. G. Frehlich, "Onset of strong scintillation with application to remote sensing of turbulence inner scale," *Appl. Optics*, vol. 35, no. 6, pp. 986–997, 1996.
[19] J. C. Ricklin, S. M. Hammel, F. D. Eaton, and S. L. Lachinova, "Atmospheric channel effects on free-space laser communication," *J. Opt. Fiber. Commun. Rep.*, vol. 3, no. 2, pp. 111–158, 2006.